Solar RRL

WILEY VCH

Solar RRL

RESEARCH ARTICLE OPEN ACCESS

Versatile Two-Step Process for Perovskite-Based Tandem Photovoltaics

Ronja Pappenberger[1,2] | Roja Singh[1,2] | Alexander Diercks[2] | Tonghan Zhao[1] | Raphael Pesch[1,2] | Julian Petry[1,2] | Daniel Baumann[1,2] | Xuzheng Liu[1,2] | Ulrich W. Paetzold[1,2]

[1]Institute of Microstructure Technology (IMT), Karlsruhe Institute of Technology (KIT), Eggenstein-Leopoldshafen, Germany | [2]Light Technology Institute (LTI), Karlsruhe Institute of Technology (KIT), Karlsruhe, Germany

Correspondence: Ronja Pappenberger (ronja.pappenberger@kit.edu) | Ulrich W. Paetzold (ulrich.paetzold@kit.edu)

Received: 17 March 2025 | **Revised:** 28 April 2025 | **Accepted:** 30 April 2025

Funding: Ministry of Science and Culture of the State of Lower Saxony: Project NextGenPV, "zukunft.niedersachsen"; European Union: NEXUS, Grant/Award Number: 101075330; Helmholtz Association: Zeitenwende; Helmholtz Association: Solar Technology Acceleration Platform (Solar TAP); Helmholtz Association: program oriented funding period IV, Materials and Technologies for the Energy Transition, Topic 1: Photovoltaics and Wind Energy, Code: 38.01.04; German Federal Ministry for Economic Affairs and Climate Action (BMWK), 27Plus6, Grant/Award Number: 03EE1056B; Karlsruhe School of Optics & Photonics (KSOP)

Keywords: 2T tandem solar cell | compositional engineering | dual passivation | perovskite solar cell | sequential deposition

ABSTRACT

Perovskite photovoltaics promise high power conversion efficiencies (PCEs) and cost-effective fabrication, making them a transformative solar technology. Among deposition methods, the solution-based two-step process has emerged as a promising approach for integrating high-quality perovskite layers onto silicon (Si) bottom cells, enabling dense and pinhole-free films. However, achieving both high efficiency and long-term stability remains underexplored for solution-based two-step-processed perovskite solar cells (PSCs). This study introduces a versatile solution-based two-step method, demonstrating a seamless transition from a triple-cation (CsMAFA) to a more stable double-cation (CsFA) perovskite composition. Implementing a novel dual bimolecular passivation strategy with propane-1,3-diammonium iodide ($PDAI_2$) and n-butylammonium iodide (BAI) for both bulk and surface passivation effectively addresses defects at grain boundaries and interfaces. This approach minimizes nonradiative recombination, enhances film crystallization, and promotes efficient charge extraction. The resulting PSCs demonstrate a stable power output of 20.9%, representing the highest reported efficiency for a solution-based two-step processed PSC with a bandgap of 1.67 eV. Laboratory-scale monolithic perovskite/Si tandem solar cells (1 cm^2 active area) achieve PCEs exceeding 26% on small-textured Si bottom cells (<2 µm). This emphasizes the potential of the solution-based two-step process for practical implementation in high-performance photovoltaic systems.

1 | Introduction

In recent years, organic–inorganic hybrid perovskite solar cells (PSCs) have attracted enormous attention as next-generation photovoltaic (PV) materials, with power conversion efficiencies (PCEs) rising impressively from 3.8% in 2009 to 26.7% today, narrowing the gap to the highest reported PCEs of market-dominating silicon (Si) solar cells [1–3]. Inverted PSCs (p–i–n architecture) are compatible with p-type Si bottom cells for monolithic perovskite/Si tandem solar cells (TSCs), enabling PCEs beyond the crystalline Si solar cell limit of 29% [4] and reaching record efficiencies of over 34% [3].

A major challenge for the commercialization of PSCs is the long-term stability, which still lags behind that of Si solar cells [5–8]. Perovskite compositions containing methylammonium (MA) – while often achieving the highest PCEs – are particularly prone to thermal degradation, compromising their long-term stability. As a result, there is growing interest on developing MA-free systems to achieve both high efficiency and enhanced long-term stability [9–14].

In parallel, surface and bulk passivation have become crucial strategies for mitigating recombination losses and improving device stability [15–19]. The top interface between the perovskite and electron transport layer (ETL) suffers from energy-level mismatch and severe nonradiative recombination losses [20–23]. In addition, bulk defects can appear in conjunction with the occurrence of grain boundaries. These imperfections facilitate ion migration and accelerate degradation under light and thermal stress [24–31].

A common approach to reduce recombination at the perovskite/ETL interface and improve device performance is the post-treatment of the perovskite film [16–19]. Evaporated lithium fluoride (LiF) is one of the most widely used physical surface passivation materials due to its compatibility with various perovskite compositions [23, 32–41]. However, literature shows that LiF negatively affects long-term operational stability [15, 33, 37, 42]. As an alternative surface passivation, Liu et al. [20] suggest a bimolecular passivation strategy. There, diammonium ligands provide a field-effect passivation, with one $-NH_3^+$ group anchoring to the perovskite surface and the other extending outward. This results in a surface dipole and n-type doping, repelling hole carriers to reduce interface recombination [20, 43–46]. In the following, propane-1,3-diammonium iodide ($PDAI_2$) is utilized as field-effect passivator. Chemical passivation is used to further reduce surface recombination. Here, a commonly used chemical passivating agent [47, 48] – n-butylammonium iodide (BAI) – is introduced and combined with $PDAI_2$.

Bulky monoammonium cations such as phenethylammonium (PEA), BA, and others are commonly used to form 2D Ruddlesden–Popper (R–P) phase perovskites to reduce nonradiative recombination in the bulk and grain boundaries of the 3D perovskite film [12, 15, 49–57]. Here, the 2D layers are held together by weak van der Waals interactions, which are not only detrimental to structural stability under harsh conditions but also generate deep quantum wells that limit charge transfer between 2D layers [58–61]. By incorporating diammonium cations such as PDA, 2D Dion–Jacobson (DJ) phase perovskites can be formed. The adjacent layers are connected by hydrogen bonding, which endows better structural stability and charge transfer ability [58, 62, 63]. However, DJ-type perovskites are less tolerant to lattice distortions, particularly in FA-based perovskite films. The large FA cations significantly distort the Pb–I octahedra and the assembly of the already distorted 2D slabs with the rigid spacer cations tends to introduce defects in the final film [64]. To maintain high film quality while balancing structural rigidity, defect tolerance, and structural stability, RP-type spacer cations can be combined with DJ-type spacer cations [58]. Herein, we use a combination of BAI and $PDAI_2$ for bulk passivation.

To achieve highly efficient monolithic 2T tandem devices, it is essential to improve the perovskite layer and to ensure effective integration with the Si bottom cell. Commercial Si bottom cells with random pyramidal textures (texture height: 2–5 μm) offer superior light-harvesting capabilities compared to their planar or polished counterparts through enhanced light incoupling and trapping [65–70]. However, such large textures pose a challenge for controlling the morphology and quality of solution-based perovskite thin films. Reducing the texture size to <2 μm offers an alternative strategy for achieving excellent light harvesting while enabling successful deposition of the perovskite film with solution-based methods [38, 66, 69, 71–78]. Among deposition techniques, the solution-based two-step method – consisting of the subsequent deposition of the Pb-containing precursor materials and the organic cations – has emerged as a promising route to process uniform and high-quality perovskite thin films on Si bottom cells [79, 80].

In this study, we introduce a versatile solution-based two-step process, offering an easy approach to tuning the perovskite composition toward a more stable double-cation (MA-free) system. This addresses the pressing need for improving both the efficiency and long-term stability of PSCs, achieving a notable PCE of 19.2% for p–i–n single-junction PSCs with a bandgap of 1.67 eV. Optimizing the double-cation PSCs by a novel dual bimolecular passivation strategy, we further enhance device performance, reaching an outstanding efficiency of 20.9% with a V_{OC} of 1.24 V and a fill factor (FF) exceeding 80%. This represents the highest reported efficiency for a solution-based two-step processed PSC with a bandgap of 1.67 eV. The optimized PSCs demonstrate good operational stability, maintaining 94% of their initial efficiency after 1000 hr of dark storage (ISOS-D1), achieving T_{80} after 400 hr of dark storage at elevated temperatures (ISOS-D2) and reaching T_{80} after 180 hr of maximum power point (MPP) tracking (ISOS-L1). Notably, this process is adaptable to both small-textured (texture height <2 μm) and large-textured (texture height ≈2–5 μm) monolithic TSCs, achieving efficiencies of up to 26.2%.

2 | Results and Discussion

The solution-based two-step method employed for fabricating the perovskite thin films in this work is illustrated in Figure 1. The device architecture of the PSCs (p–i–n) is displayed in Figure 1a and consists of the layer stack glass/ITO/NiO_x/2PACz/perovskite/surface passivation/C_{60}/BCP/Ag. For the TC perovskite film (labeled as TC) with the nominal composition $Cs_{0.16}MA_{0.06}FA_{0.78}Pb(I_{0.79}Br_{0.21})_3$ and a bandgap of 1.68 eV (Figure S1a), an established recipe from our previous work [32] is utilized. The process steps are displayed in Figure 1b, using LiF for surface passivation. Replacing methylammonium iodide (MAI) with formamidinium iodide (FAI) in the perovskite precursor materials results in a DC perovskite film (labeled as DC) with the nominal composition $Cs_{0.16}FA_{0.84}Pb(I_{0.79}Br_{0.21})_3$. The addition of methylammonium chloride (MACl) improves the crystallization of the perovskite film, but evaporates in the final annealing step [81]. Similar to the TC perovskite film, LiF is used here for surface passivation (Figure 1c). To enhance the PSC performance of the DC perovskite film, a dual bimolecular passivation strategy is developed. Here, a combination of $PDAI_2$ and BAI is incorporated into the organic precursor solution (bulk passivation) and used for surface passivation instead of LiF (Figure 1d, labeled as DC opt.). Further details on the fabrication method of the PSCs are described in the Experimental Section.

2.1 | Photovoltaic Performance of Perovskite Solar Cells

An optimized, dual-passivated DC perovskite is identified in the following as a superior strategy for achieving highly efficient and stable p–i–n type PSCs.

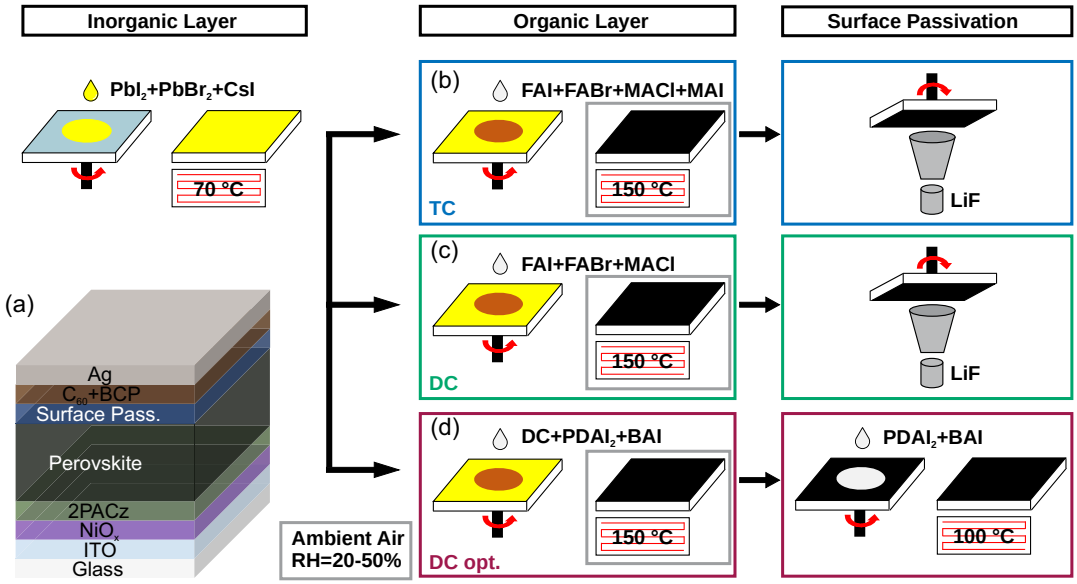

FIGURE 1 | (a) Schematic of the PSC architecture (p–i–n architecture) used in this study. Schematic illustration of the employed solution-based two-step deposition method for fabrication of the (b) TC perovskite films, (c) DC perovskite films, and (d) optimized double-cation perovskite films (DC opt.). TC and DC PSCs use LiF for surface passivation. DC opt. PSCs use a combination of $PDAI_2$+BAI for bulk and surface passivation. DC = double cation; PSCs = perovskite solar cells; TC = triple cation.

Changing the perovskite composition from a TC to a DC is straightforward and enhances the V_{OC} while reducing the hysteresis of the PSCs, as indicated by the statistical results and current density–voltage (J–V) characteristics (Figure 2a and Table S1). This improvement results in a champion performance of 19.2% in the backward scan (18.3% in the forward scan) with a V_{OC} of 1.21 (1.20) V, a J_{SC} of 20.0 (19.9) mA cm^{-2}, and FF of 79.4% (76.8%) of the DC PSCs. Based on a statistical analysis using the Welch's *t test* [82], the improvement in V_{OC} is statistically significant (Table S2) and is not due to an increase in the bandgap (Figure S1a).

Optimizing the DC perovskite composition (DC opt.) with a dual-passivation strategy – using a bimolecular passivation with $PDAI_2$ and BAI for both bulk and surface passivation – significantly enhances the V_{OC}, FF, and J_{SC} compared to the DC PSCs

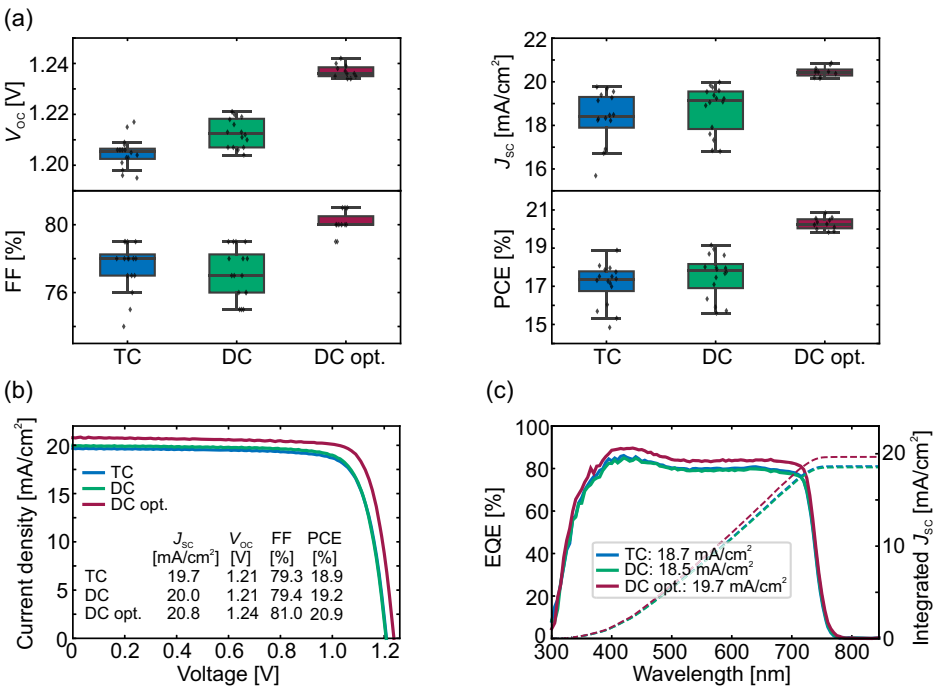

FIGURE 2 | (a) Statistical distribution (in total 43 devices) of the open-circuit voltage (V_{OC}), FF, short-circuit current density (J_{SC}), and PCE, (b) current density versus voltage (J–V) characteristics, and (c) EQE as well as the corresponding integrated J_{SC} for opaque PSCs with the TC, the DC, and the optimized double cation (DC opt.) recipe. DC = double cation; EQE = external quantum efficiency; FF = fill factor; TC = triple cation.

as confirmed by Welch's *t test* (Table S2). This results in a remarkable improvement in device performance, achieving a PCE of 20.9% (19.8%), a V_{OC} of 1.24 (1.22) V, a J_{SC} of 20.8 (20.7) mA cm^{-2}, and FF of 81.0% (78.3%) for the champion PSC (Figure S2c). Particularly striking is the enhancement in V_{OC} by an average of 20–30 mV, which is not governed by an increase in bandgap (Figure S1a) but associated with reduced nonradiative recombination, as discussed further in the subsequent section. The reduced standard deviation of the statistical results suggests an improved repeatability of the optimized DC PSCs.

While both perovskite compositions – TC and DC – exhibit a similar external quantum efficiency (EQE), the EQE of the optimized DC PSCs demonstrates a substantial improvement over the entire spectral range (Figure 2c). Given that both the device architecture and the absorption spectra (Figure S1b) remain comparable across all devices, the increase in EQE can be attributed to an improved charge carrier extraction. This leads to an enhancement in the integrated J_{SC} by around 1 mA cm^{-2} to 19.7 mA cm^{-2} for the optimized DC perovskite.

To investigate the impact of dual passivation compared to single passivation, devices are fabricated with bimolecular passivation applied either solely in the bulk or solely at the surface of the perovskite film (Figure S3). When bimolecular passivation is solely used in the bulk (with LiF for surface passivation), the V_{OC} is reduced by approximately 30 mV compared to the DC PSCs, leading to a lower overall PCE. In contrast, devices with bimolecular passivation introduced solely at the surface (without bulk passivation) achieve high PCEs, with notable improvements in V_{OC}, FF, and J_{SC}. Strikingly, the dual-passivation strategy can even further boost the FF by approximately 4% and the J_{SC} by around 0.5 mA cm^{-2}, resulting in the highest device performance.

It is important to emphasize that the concentration of the bimolecular passivation plays a decisive role. For bulk passivation, it is essential to balance the trade-off between V_{OC} loss and the gains in J_{SC} and FF, with the optimum concentration being reduced to 0.1 mg mL^{-1} (Figure S4). For surface passivation, exceeding the optimum concentration results in a further increase in V_{OC}, but the FF drops sharply, likely due to the insulating effect of a thicker 2D passivation layer at the surface (Figure S5) [15, 52, 53, 83–85]. If the concentration is too low, both FF and J_{SC} show no improvement compared to the DC PSCs (Figure S6).

Further investigations comparing the bimolecular passivation strategy to the more commonly used monomolecular passivation [45, 86–90] reveal that bimolecular passivation – as previously explored by Liu et al. [20] – outperforms in both bulk and surface passivation, leading to superior FF and J_{SC} (Figures S7–S10).

So far, the bimolecular passivation has been incorporated via the organic cation solution. Given the sequential deposition of Pb-containing precursor materials and organic cations in the two-step process, bulk passivation can in principle be introduced in both deposition steps. However, experiments show that efficiency improvement is only observed when bimolecular passivation is introduced into the organic cation solution (Figure S11). Without further optimization, the dual bimolecular passivation strategy can also be successfully implemented to TC PSCs (Figure S12), demonstrating the versatility of the passivation.

In summary, the simultaneous improvement in V_{OC} and FF for the optimized DC devices with bimolecular passivation is remarkable, underscoring the critical importance of dual passivation at both theperovskite/C_{60} interface and the grain boundaries of the perovskite thin films.

2.2 | Material and Photophysical Characteristics

The optoelectronic properties of the TC, DC, and optimized DC perovskite films are investigated using intensity-dependent photoluminescence quantum yield (PLQY) measurements (Figure S13a). The "implied V_{OC}" (V_{OC-imp}) can be calculated from the internal quasi-Fermi-level splitting (QFLS) according to Stolterfoht et al. [91] and Fassl et al. [92] (Figure S13b). Nonradiative recombination sites, where charge carriers are lost without photon emission, are detrimental to solar cell performance. Typically, they occur at defect sites within the bulk or at interfaces, reducing the V_{OC} and overall device efficiency. Therefore, minimizing these recombination losses is essential for improving both the efficiency and stability of PSCs.

By plotting the calculated V_{OC-imp} against light intensity, the internal ideality factor (n_{id}) can be determined, providing insights into the trap-state density [91, 93–96]. Half-stack devices with and without ETL – here C_{60} – are prepared. Analysis of the half-stack devices without C_{60} (ITO/NiO_x/2PACz/perovskite) gives information about the quality of the perovskite bulk. A comparison between TC and DC perovskite films shows a reduction in n_{id} from 1.59 for the TC perovskite films to 1.55 for the DC perovskite films (Figure 3a). This indicates that changing the perovskite composition improves the quality of the perovskite bulk. Implementing the dual bimolecular passivation strategy further reduces the n_{id} to 1.28 (DC opt.), effectively lowering the trap-state density. Adding the C_{60} layer reveals a similar trend (Figure 3b), with the DC perovskite films exhibiting a lower n_{id} factor (1.62) compared to the TC perovskite films (1.65), indicating a higher concentration of nonradiative recombination centers at the interface in the latter. The optimized DC perovskite films exhibit the lowest n_{id} value (1.39), demonstrating that the dual bimolecular passivation strategy is highly effective in minimizing nonradiative recombination at the perovskite/C_{60} interface. This result is consistent with the improved FF and V_{OC} obtained from the statistical results of the optimized DC PSCs (Figure 2a,b and Table S1).

To analyze the crystal structure of the perovskite films, X-ray diffraction (XRD) measurements are performed (Figure 3c). All three perovskite films exhibit diffraction peaks at ≈13.7°, ≈19.6°, ≈24.2°, and ≈28.1°, corresponding to the (100), (110), (111), and (200) crystal planes of the 3D perovskite, respectively. The diffraction peak at ≈12.2° can be attributed to unreacted PbI_2 [15, 50, 97, 98]. The DC perovskite films show an increased ratio of the (100) perovskite peak to the PbI_2 peak compared to the TC perovskite films (Figure S14a), indicating less unreacted PbI_2. The optimized DC perovskite films exhibit an even higher (100) perovskite peak-to-PbI_2 peak ratio, demonstrating the most efficient conversion to the final perovskite phase. For the DC and

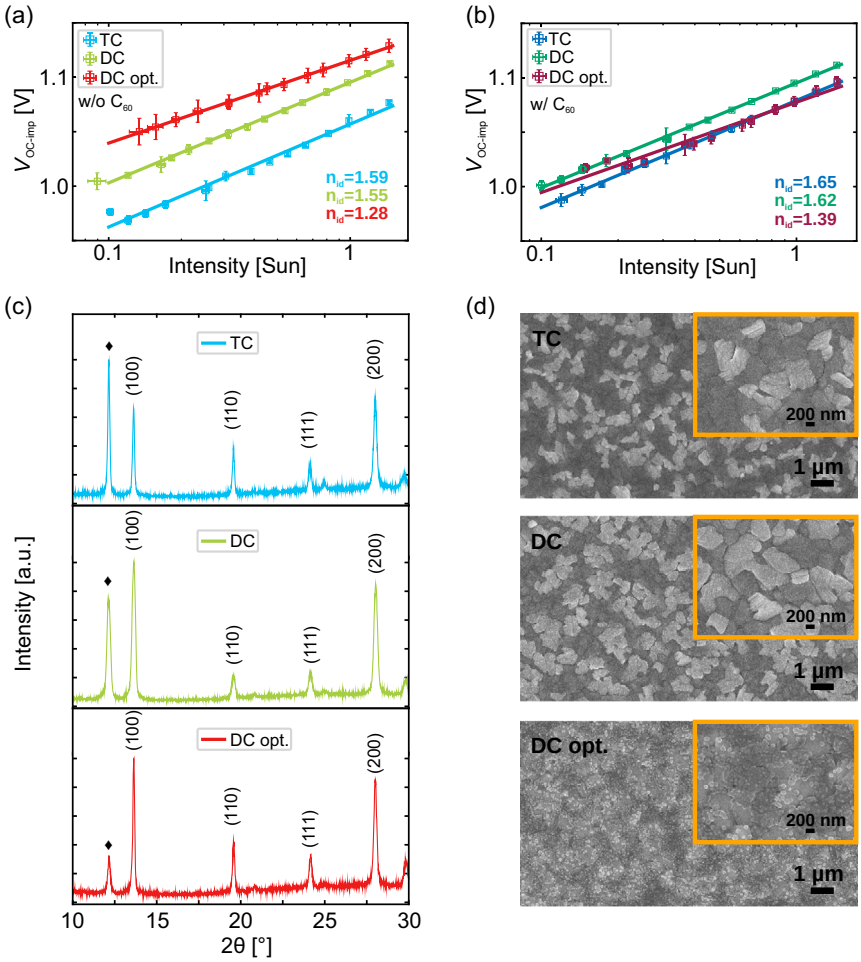

FIGURE 3 | Ideality factor (n_{id}) extracted from a fit to the implied V_{OC} (V_{OC-imp}) measured (a) without and (b) with C_{60} as ETL, (c) XRD pattern (◆ denotes the PbI_2 phase), and (d) top-view SEM images of the perovskite films with the TC, the DC, and the optimized double cation (DC opt.) recipe fabricated on ITO/NiO_x/2PACz substrates. (a) and (b) are measured from the HTL side. DC = double cation; TC = triple cation; SEM = scanning electron microscopy; XRD = X-ray diffraction.

optimized DC perovskite films, the ratio of the (100) diffraction peak intensity to the other diffraction peak intensities (Figure S14a) is notably increased, indicating that the DC and optimized DC perovskite films are grown with (100)-preferred orientation.

Analysis of the full width at half maximum (FWHM) of the (100) perovskite peak (Figure S14b) shows a lower value for the optimized DC perovskite film (0.16°) compared to the DC perovskite film (0.23°). The reduced FWHM value indicates an enhanced crystallinity and larger grain size of the perovskite film according to the Scherrer equation [99, 100].

In grazing-incidence wide-angle X-ray scattering (GIWAXS) measurements, no peaks are observed for the optimized DC perovskite films at low scattering vectors q (Figure S15), indicating that either the addition of $PDAI_2$ and BAI to the perovskite bulk results in a concentration too low to form a 2D perovskite phase or that the layer is too thin to be detected [101, 102]. The pole figure of the (100) perovskite peak highlights differences in orientation distribution (Figure S16). TC perovskite films exhibit stronger scattering at 10°, while both TC and DC perovskite films are predominantly oriented at 60°. Bulk-passivated DC perovskite films present a double peak at 40° and 70°, whereas optimized DC perovskite films demonstrate the strongest scattering at 70°. The optimized DC perovskite films exhibit the most vertical crystal orientation, which could explain the improved charge carrier transport [103, 104].

The surface morphology of the perovskite films is studied by scanning electron microscopy (SEM) and atomic force microscopy (AFM). According to the SEM images (Figures S3d and S17), TC, DC, and bulk-passivated DC perovskite films exhibit a comparable surface morphology. The grains that appear brighter in SEM are attributed to unreacted PbI_2, which is observable in line with XRD results. With the introduction of $PDAI_2$ and BAI for surface passivation, the DC perovskite films show a distinctive lamellar morphology with less apparent grain boundaries and reduced bright grains. This indicates the formation of a 2D capping layer on top of the 3D perovskite film [105], which helps to convert more unreacted PbI_2. The 2D capping layer does not fully cover the underlying layer, but accumulates along the grain boundaries, potentially enhancing the charge transfer.

No significant changes in the root–mean-square (RMS) surface roughness for TC, DC, and optimized DC perovskite films are observable in the AFM images (Figure S18). In accordance to

the FWHM, the bulk-passivated DC perovskite films show enlarged grain sizes compared to the DC perovskite films.

Materials characterization reveals that dual bimolecular passivation reduces nonradiative recombination losses at the perovskite/C_{60} interface as well as grain boundaries and results in an improved film quality of the perovskite layer.

2.3 | Stability

The operational stability of PSCs is affected by several stress factors such as light [106, 107], elevated temperatures [108–110], ambient environment (oxygen, humidity) [111–113], and electrical bias [114–116]. In order to understand the degradation mechanisms triggered by different stress factors, three standardized tests are chosen for understanding the role of light (ISOS-L1: 100 mW cm^{-2}, 25°C, MPP tracking), dark storage (ISOS-D1: dark, 25°C, intermittent *J*–*V*), and elevated temperatures (ISOS-D2: dark, 85°C, intermittent *J*–*V*) on PSCs [117]. Semitransparent devices with the layer stack glass/ITO/NiO_x/2PACz/perovskite/surface passivation/C_{60}/SnO_x/IZO/Au are exposed to the test conditions.

To examine the effect of dark storage on stability, semitransparent devices are stored under ISOS-D1 test conditions for 1000 hr. The normalized PCE from intermittent *J*–*V* measurements for TC, DC, and optimized DC PSCs is shown in Figure 4a. It is noteworthy that the optimized DC devices are stable over a period of 1000 hr, while the TC and DC devices show a deterioration in device performance (≈30% loss for TC and ≈15% loss for DC PSCs). Interestingly, both TC and DC devices exhibit a significant performance drop during the first 200 hr, followed by a stable output over the remaining 800 hr. The TC devices reach T_{80} after 130 h, whereas the DC devices stabilize at the T_{80} threshold. Figure S19 illustrates that the decline in FF and J_{SC} for both the TC and DC devices is the main reason for the reduced PCE. While the V_{OC} remains stable for the DC and optimized DC devices, the TC devices experience a noticeable V_{OC} loss of ≈3%.

To assess the impact of elevated temperatures on the stability of dark-stored PSCs, accelerated aging tests on semitransparent devices are conducted under ISOS-D2 test conditions for 1000 hr. The normalized PCEs from intermittent *J*–*V* measurements for TC, DC, and optimized DC are shown in Figure 4b. It is evident that elevated temperatures have a profound impact on stability. The TC devices exhibit the most significant performance degradation, reaching T_{80} after 250 hr. The DC and optimized DC devices behave similarly over a period of 1000 hr with a T_{80} time of 400 hr. Considering the remaining device parameters, Figure S20 reveals that the decrease in FF is the primary factor behind the decline in PCE, with a loss of approximately 45% for TC devices and around 30% for DC and optimized DC devices. Interestingly, while the V_{OC} is rather staying constant for the optimized DC devices (≈3% loss), a more severe drop can be observed for the TC (≈6% loss) and DC (≈5% loss) devices. From literature it is known that prolonged exposure to elevated temperatures (over a period of 500 hr) results in increased nonradiative recombination, either within the perovskite layer or at the interfaces to the charge transport layers, leading to a reduction in both FF and V_{OC} [118–120].

To evaluate the operational stability of the PSCs not only under dark storage conditions but also under light exposure, the semitransparent PSCs are subjected to ISOS-L1 test conditions for

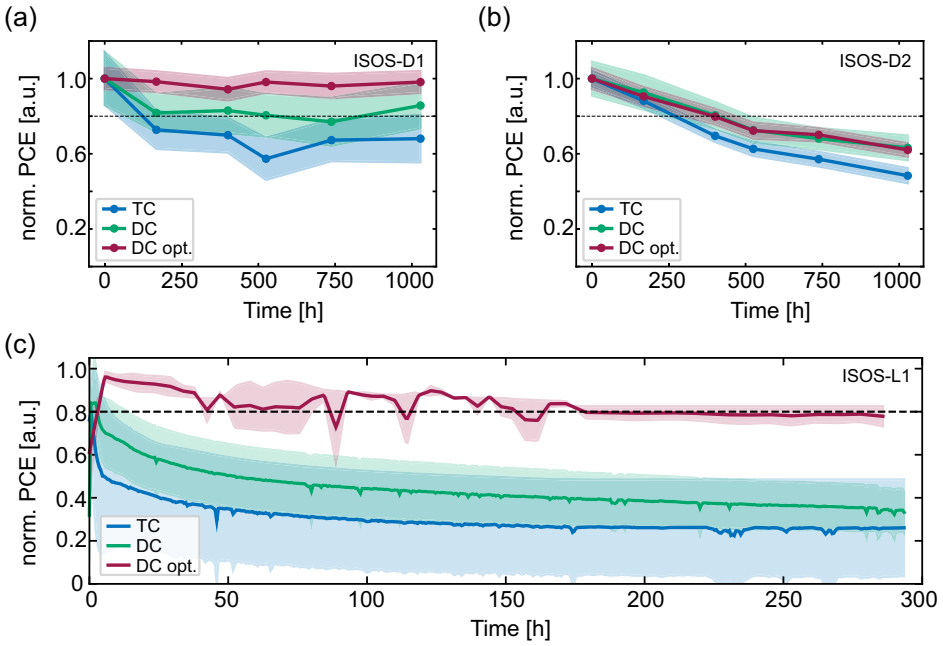

FIGURE 4 | Normalized PCE from *J*–*V* measurements of semitransparent TC, DC, and optimized double cation (DC opt.) PSCs under (a) ISOS-D1 testing conditions (dark, 25°C, intermittent *J*–*V*) and under (b) ISOS-D2 testing conditions (dark, 85°C, intermittent *J*–*V*) for 1000 hr. (c) Normalized PCE at the MPP tracking of semitransparent TC, DC, and DC opt. PSCs under ISOS-L1 test conditions (100 mW cm^{-2}, 25°C, MPP tracking) for 300 hr. The data fluctuations originate from the measurement setup. DC = double cation; MPP = maximum power point; PCE = power conversion efficiency; TC = triple cation.

300 hr (Figure 4c). Similar to the ISOS-D1 test conditions, TC PSCs demonstrate a rapid performance drop within the first 5 hr, followed by a more gradual decline over the subsequent 295 hr. The DC PSCs exhibit a comparable behavior but maintain a higher performance level throughout the 300 hr period. In contrast, the optimized DC PSCs display the most stable performance, showing an initial light-soaking effect within the first 5 hr and achieving T_{80} after 180 hr. Analyzing the remaining device parameters, Figure S21 shows that the primary contributor to the decline in PCE is the reduction in J_{SC}, while the V_{OC} remains constant across all devices.

It is important to note that LiF – used for surface passivation in both TC and DC devices – may also contribute to degradation [15, 33, 37, 42]. However, this effect cannot be distinguished in the current analysis.

In summary, the degradation mechanisms observed under various stress conditions reveal that transitioning to an MA-free perovskite composition enhances the operational stability of PSCs. Additionally, using a dual bimolecular passivation strategy can further improve their long-term stability. However, the stability aspect still necessitates additional optimization, as the results have not yet reached state-of-the-art stability metrics [121].

2.4 | Textured 2T Tandem Devices

After successfully testing the dual bimolecular passivation strategy on single-junction PSCs, the process is implemented on Si bottom cells to fabricate monolithic perovskite/Si TSCs. The device architecture of the TSCs consists of the layer stack Si/ITO/NiO_x/2PACz/perovskite/$PDAI_2$+BAI/C_{60}/SnO_x/IZO/Ag/MgF_2 with an active area of 1.0 cm^2. While the Si PV industry predominantly utilizes random pyramidal textures with a peak-to-valley distance of ≈5 μm for optimal light management [122–125], such large textures are not easily compatible with solution-processed perovskite thin films [15, 71, 72]. To balance light harvesting with solution-process compatibility, submicrometer pyramidal textures (<2 μm) have been proposed as a viable compromise [38, 65, 78, 126].

The developed dual bimolecular passivation strategy demonstrates high performance on planar Si bottom cells, reaching an efficiency exceeding 26% (Figure S22a), which remains competitive with the highest reported values for solution-based two-step processed perovskite/Si TSCs [79]. Given the potential of the two-step method in producing uniform, high-quality perovskite films on textured Si bottom cells, the following sections focus on its application in textured 2T TSCs.

Although conventional solution-based processes typically fail to produce functional perovskite layers on large pyramidal textures, an initial test is performed using Si bottom cells with a pyramid height distribution of approximately 2–5 μm (labeled as large-textured). The *J–V* characteristic and EQE response of the champion device are depicted in Figure S23, with the best 2T tandem device reaching a PCE of 24.1%. The device performance is primarily constrained by a low FF. Furthermore, the EQE spectra show a current mismatch of 1.5 mA cm^{-2}, indicating that the TSC is top limited. The lower J_{SC} of the PSC is likely due to the thick perovskite layer, making charge carrier extraction challenging [127–130]. Cross-sectional SEM images confirm that the two-step process successfully enables perovskite coverage on textures of 2 μm in height (Figure S23c). However, further investigation revealed that some of the Si bottom cells featured pyramidal outlayers exceeding 5 μm in height (Figure S23d). While such outliers are not present on every Si bottom cell, their occurrence poses an additional challenge for achieving complete perovskite coverage via solution processing. These features explain the incomplete coverage observed in top-view SEM images, potentially increasing susceptibility to shunting (Figure S23e). Nevertheless, the results demonstrate the feasibility of fabricating perovskite films even on large-textured Si bottom cells (2–5 μm) using the solution-based two-step method, while also highlighting the need for further processing advancements to optimize device performance.

Reducing the pyramid height to below 2 μm results in a PCE of 26.2% (25.9%), a V_{OC} of 1.83 (1.83) V, a J_{SC} of 18.6 (18.6) mA cm^{-2}, and FF of 76.6% (76.2%) for the champion TSC (Figure 5). The EQE spectra reveal a current mismatch of 1.1 mA cm^{-2}, indicating that the TSC is bottom limited. Consequently, further advancements in light management are essential for future efficiency improvements. While still below record values [3], this represents the highest efficiency reported to date for a solution-based two-step processed TSC on small-textured silicon bottom cells. SEM images confirm complete perovskite coverage on submicrometer pyramidal textures (Figure S24a). Short-term stability is verified by MPP tracking for 5 min (Figure S24b).

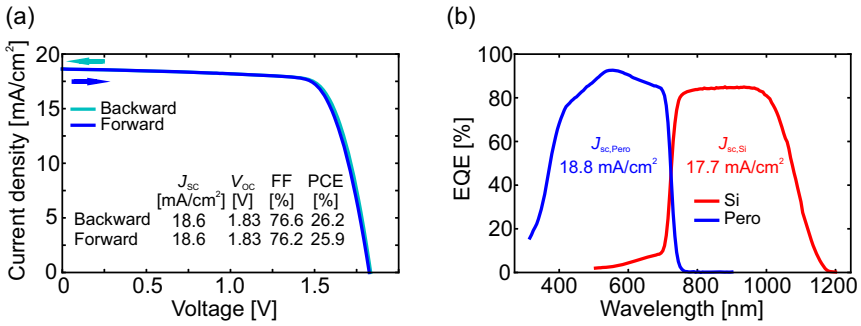

FIGURE 5 | (a) Current density versus voltage (*J–V*) characteristics and (b) EQE of the champion small-textured monolithic 2T TSC (active area: 1.0 cm^2, pyramid height ≈0.5–1 μm) with a perovskite bandgap of E_g = 1.67 eV (DC opt. perovskite) and with 100 nm of MgF_2 as antireflective coating. EQE = external quantum efficiency; TSC = tandem solar cell.

These results highlight the adaptability of the developed passivation strategy across different pyramidal texture heights in 2T TSCs, reinforcing its potential for broader implementation in high-efficiency perovskite/Si tandem PV. As this work serves as a proof of concept, further developments – such as improved light management and precise bandgap tuning – are essential to realize maximal device efficiencies.

3 | Conclusion

This work introduces a versatile solution-based two-step process that facilitates an easy transition from TC to DC perovskite composition, offering enhanced V_{OC} and improved device stability. The incorporation of a novel dual bimolecular passivation strategy with $PDAI_2$ and BAI for both bulk and surface passivation effectively addresses nonradiative recombination at the perovskite/C_{60} interface and mitigates defects at grain boundaries. The optimized perovskite film morphology results in more efficient charge carrier extraction and elevates device performance, achieving a remarkable efficiency increase from 19.2% up to 20.9% with a V_{OC} of 1.24 V and a FF exceeding 80%. To the best of our knowledge, this is the highest reported efficiency for a MA-free p–i–n type PSC with a bandgap of 1.67 eV processed using a solution-based two-step method, approaching the current record efficiency for wide-bandgap MA-free PSCs of 21.3% [131]. Moreover, the dual bimolecular passivation strategy significantly enhances operational stability, reaching T_{80} after 180 hr of MPP tracking. Implementing the process on textured monolithic perovskite/Si TSCs (active area of 1 cm^2) results in PCEs up to 26.2%, marking the highest reported efficiency for solution-based two-step processed TSCs on small-textured Si bottom cells. Overall, this work highlights the potential of compositional engineering with MA-free perovskite systems and strategic defect management using advanced passivation techniques, paving the way for the development of high-efficiency, stable p–i–n PSCs, and TSCs using the solution-based two-step method.

4 | Experimental Section

4.1 | Materials

2PACz (TCI, CAS: 20999-38−6), lead iodide (PbI_2: TCI, CAS: 10101-63−0), lead bromide ($PbBr_2$: TCI, CAS: 10031-22−8), formamidinium iodide (FAI: Greatcell solar materials, CAS: 879643-71−7), formamidinium bromide (FABr: Dyenamo, CAS: 146958-06−7), methylammonium iodide (MAI: Dyenamo, CAS: 14965-49−2), methylammonium chloride (MACl: Dyenamo, CAS: 593-51−1), cesium iodide (TCI, CAS: 7647-17−8), fullerene-C_{60} (C_{60}: Sigma–Aldrich, CAS: 99685-96−8), bathocuproine (BCP: Lumtec, CAS: 4733-39−5), magnesium fluoride (MgF_2: Sigma–Aldrich, CAS: 7783-40−6), lithium fluoride (LiF: ChemPur, CAS: 7789-24−4), n-butylammonium iodide (BAI: Greatcell solar materials, CAS: 36945-08−1), propane-1,3-diammonium iodide ($PDAI_2$: Greatcell solar materials, CAS: 120675-53−8) were used. All solvents including N, N-dimethylformamide, 99.8% (DMF, CAS: 68-12−2), dimethyl sulfoxide anhydrous, ≥99.9% (DMSO, CAS: 67-68−5), 2-propanol, 99.5%, (IPA, CAS: 67-63−0), and ethanol absolute anhydrous, ≥99.8%, (EtOH, CAS: 64-17−5) were ordered from VWR Chemicals.

4.2 | Perovskite Solution Preparation

The TC perovskite ($Cs_{0.16}FA_{0.78}MA_{0.06}Pb(I_{0.79}Br_{0.21})_3$) solution was prepared according to our previous work [32]. Two different solutions were prepared. For the inorganic solution, 1.275 M PbI_2 and 0.225 M $PbBr_2$ were dissolved in 1 mL DMF:DMSO (9:1 volume ratio, v:v; less DMSO, since it was added with the CsI solution) and heated up to 130°C for 30 min to completely dissolve the materials. After cooling down, 70 µL CsI solution (corresponds to 7 mol% CsI, 390 mg mL^{-1} CsI in DMSO) was added to the inorganic solution. The organic cation solution was prepared by dissolving FAI (51.6 mg), FABr (27.9 mg), MAI (6.4 mg), and MACl (9 mg) in 1 mL IPA. The addition of MACl improved the crystallization of the perovskite film but evaporated in the final annealing step [81].

For the DC perovskite ($Cs_{0.16}FA_{0.84}Pb(I_{0.79}Br_{0.21})_3$) solution, the inorganic solution was prepared as mentioned before for the TC perovskite. The organic cation solution was prepared by dissolving FAI (58.5 mg), FABr (27.9 mg), and MACl (9 mg) in 1 mL IPA.

For the optimized DC perovskite, a bimolecular passivation containing 0.1 mg mL^{-1} $PDAI_2$ and 0.1 mg mL^{-1} BAI dissolved in IPA was added to the organic cation solution for bulk passivation.

4.3 | Single-Junction (SJ) Perovskite Solar Cell Fabrication

The planar p–i–n PSCs with the layer stack glass/ITO/NiO_x/2PACz/perovskite/surface passivation/C_{60}/BCP/Ag were fabricated as follows. The glass substrates with 120 nm-thick indium tin oxide (ITO) coating (sheet resistance 15 Ω cm^{-2}, Luminescence Technology, CAS: 50926-11−9) were cut in 16 mm × 16 mm and cleaned in an ultrasonic bath with deionized water with glass cleaner, acetone, and IPA for 10 min each. This was followed by 3 min of oxygen plasma treatment before the deposition of the hole transport layer (HTL). For the HTL layer, a 5 nm-thick NiO_x film was sputtered from a NiO_x target using 100 W power with pure Ar at 1 mTorr on the ITO substrate. Then, a thin layer of 2PACz was deposited on the ITO/NiO_x substrate by spin coating at 3000 rpm for 30 s and subsequently annealed at 100°C for 10 min. The 2PACz precursor solution was prepared by dissolving 2PACz in anhydrous EtOH with a concentration of 0.375 mg mL^{-1}. The prepared solution was placed in an ultrasonic bath for at least 20 min before use. All perovskite absorber layers were deposited on the substrate using the two-step deposition method. The first step was the deposition of the inorganic PbI_2 layer. This was achieved by dropping 60 µL of the inorganic solution and spin coating at 1500rpm for 30 s. The films were subsequently annealed at 70°C for 1 min resulting in a yellow-transparent layer. The formation of the perovskite was achieved by dropping 80 µL of the cation solution on top of the inorganic layer and rapidly starting the spin-coating process at 2500 rpm for 30 s, which resulted in a red film. This was followed by an annealing step at 150°C for 15 min outside of the glovebox under ambient conditions (at a relative humidity of 20–50%), converting it to the desired black perovskite film. It has to be noted that the spin-coating process took place in N_2-filled glovebox. For the second annealing step, a transport box was used to transfer the samples

out of the glovebox in order to keep the samples in a nitrogen atmosphere right before the annealing on a preheated plate (150°C). As soon as the transport box was opened, the crystallization and phase-change process started and a rapid transfer to the hotplate directly after opening the transport box was beneficial for the cell performance [132]. After annealing, 1 nm LiF was thermally evaporated at an evaporation rate of 0.1–0.2 Å s^{-1} at a pressure of around 10^{-6} mbar for the TC and DC perovskite films. For the optimized DC perovskite films, 100 µL of a bimolecular passivation containing 1.25 mg mL^{-1} $PDAI_2$ and 1.25 mg mL^{-1} BAI dissolved in IPA was dynamically spin coated on the perovskite films at 4500 rpm for 30 s, followed by annealing at 100°C for 5 min. As electron transport (ETL) layer, 20 nm of C_{60} and 5 nm of BCP were thermally evaporated and deposited using an Angstrom evaporation system at an evaporation rate of 0.1–0.2 Å s^{-1} at a pressure of around 10^{-6} mbar. Subsequently, 100 nm Ag was thermally evaporated using a shadow mask to define the active area to 10.5 mm^2 and complete the PSCs with 4 pixels per substrate. For measuring with the solar simulator, a shadow mask with an area of 7.84 mm^2 was used. For stability measurements, semitransparent devices with the layer stack glass/ITO/NiO_x/2PACz/perovskite/surface passivation/C_{60}/SnO_x/IZO/Au were prepared. Due to problems with the quality of the NiO_x layer, only 2PACz was used for ISOS-L1 measurements as the HTL. Up to the C_{60} layer, all layers were the same as for the opaque devices. The C_{60} layer was followed by a 20 nm SnO_2 layer prepared by atomic layer deposition (ALD). Subsequently, 90 nm sputtered IZO was deposited and 75 nm Au was thermally evaporated using a shadow mask. For measuring with the solar simulator, a shadow mask with an area of 9.28 mm^2 was used.

4.4 | Perovskite/Silicon Tandem Solar Cell Fabrication

Before depositing the HTL, the silicon cells were cleaned with acetone and IPA in a spin-coater process. For the HTL layer, a 15 nm (5 nm for planar Si bottom cells)-thick NiO_x film was sputtered from a NiO_x target using 100 W power with pure Ar at 1 mTorr on the silicon bottom cell with ITO layer. This was followed by a thin 2PACz layer deposited as mentioned above with a higher concentrated 2PACz solution with 0.475 mg mL^{-1}. The perovskite absorber layer was fabricated as previously described, using the same solution (1.5 M) for planar Si bottom cells and higher concentrated solutions of 1.7 M for small textures and 1.9 M for large textures. It is important to note that increasing the molarity causes a slight shift in the bandgap (Figure S25a). Bulk passivation followed the same approach as for SJ cells but was adjusted to match the perovskite solution molarity. For planar and small textured Si bottom cells, the concentration of the surface passivation was the same as for SJ cells. For large textured Si bottom cells, the concentration was reduced to 0.3 mg mL^{-1} for $PDAI_2$ and 0.3 mg mL^{-1} for BAI. For the ETL layer, 20 nm of C_{60} was thermally evaporated at an evaporation rate of 0.1–0.2 Å s^{-1} at a pressure of around 10^{-6} mbar. A 20 nm SnO_2 layer prepared by ALD was used as buffer layer. Subsequently, 90 nm sputtered IZO (45 nm IZO for large textures) was used as a transparent electrode and the active area of 1.04 cm^2 was defined by the thermally evaporated Ag electrode (300 nm for small textures and planar Si bottom cells, 600 nm with 3 × 100 µm gridfingers for large textures). In order to reduce the reflection losses, 100 nm MgF_2 as an antireflection layer was evaporated on top of the Ag. For measuring with the solar simulator, a shadow mask with an area of 1.0 cm^2 was used.

4.5 | Solar Cell Characterization

The *J*–*V* characteristics of the SJ PSCs were measured with a class AAA xenon-lamp solar simulator (Newport Oriel Sol3A) with a scan rate set at 0.6 V s^{-1} using a sourcemeter (Keithley 2400) with an air-mass 1.5 global (AM1.5G) spectra (100 mW cm^{-2}). The solar simulator irradiation intensity was calibrated using a certified silicon solar cell (Fraunhofer ISE) equipped with a KG5 bandpass filter (Schott). The MPP tracking was performed under a class AAA light emitting diode (LED)-based solar simulator (Wavelabs, LS-2), while the temperature of the devices was controlled at 25°C. The spectrum was a close match to that of AM1.5G over the relevant spectral range. The measurement was performed in a N_2-filled glovebox. The *J*–*V* characteristics of the perovskite/silicon TSCs were measured with a class AAA LED-based solar simulator (Wavelabs, LS-2) with a scan rate set at 0.6 V s^{-1} using a sourcemeter (Keithley 2400) with an air-mass 1.5 global (AM1.5G) spectra (100 mW cm^{-2}). The solar simulator irradiation intensity was calibrated using a certified silicon solar cell (Fraunhofer ISE). The measurement was performed in ambient atmosphere. To evaluate the data, a mismatch factor was determined from the EQE curve and the solar simulator spectrum and the *J*–*V* curves were corrected accordingly. The EQE was measured using a PVE300 PV QE system (Bentham EQE system). A chopping frequency in the range of 560–590 Hz with an integration time of 500 ms (750 ms for 2T tandems) to acquire the spectra in a wavelength range from 300 to 850 nm (300 to 1200 nm for 2T tandems) was used. An illumination spot (0.74 mm for SJ, 2.0 mm^2 for 2T tandems) was utilized to obtain the average over possible variations in the EQE spectra. The bandgap of all processed perovskite thin films was determined based on the differential of the EQE curves near the absorption edge (maximum of d (EQE)/d (E)) according to Krückemeier et al. [133].

4.6 | Perovskite Film Characterization

SEM analyses were carried out in a scanning electron microscope (Zeiss LEO1530) with an in-lens detector and a aperture size of 20–30 µm. For cross-sectional analyses, the cross sections were covered with a 3 nm-thick platinum layer deposited by sputtering to prevent charging. The applied acceleration voltages for surface and cross sectional analyses ranged between 5 and 10 kV. AFM images were obtained using a Nano Wizard II (JPK Instruments). The scanning area was 5 µm × 5 µm. For each parameter, 2–3 measurements were conducted, and the average RMS value was determined. Transmittance and reflectance spectra of the perovskite thin films were measured using a PerkinElmer Lambda1050 spectrophotometry setup equipped with a double-monochromator and a modulated source. A chopper frequency of 46 Hz was applied. The crystal structure of the perovskite layers was carried out utilizing XRD (Bruker D2 Phaser system) with Cu Kα radiation (λ = 1.5405 Å) in Bragg–Brentano configuration using a LynxEye detector. The XRD was taken from the

perovskite layer deposited on the ITO/NiO_x/2PACz substrate to obtain the same perovskite nucleation as well as crystallization as in the solar cells. The crystallite size D depending on the FWHM can be calculated according to the Scherrer equation

$$D = \frac{K\lambda}{\beta \cos(\Theta)} \quad (1)$$

where K is a constant, λ the X-ray wavelength, β the FWHM, and Θ the diffraction angle [99, 100]. The GIWAXS measurements were carried out on a Bruker D8 Advance equipped with a Cu X-ray source (40 kV, 40 mA), a Goebel mirror, a 0.5 mm micromask, a 0.3 mm snout on the primary track, and an Eiger2 R 500K 2D detector on the secondary track. The incidence angle was fixed at 1.5°. First, all acquired images were projected onto a virtual detector directly behind the real goniometer circle using a home-developed program in MATLAB [134]. For reshaping the experimentally acquired data into 2D diffractograms in reciprocal space, the open-access software GIXSGUI was used [135]. PLQY measurements were carried out using a LuQY Pro setup from QYB. The samples were mounted inside an integrating sphere in ambient air and a green laser ($\lambda = 532$ nm) was directed into the sphere via a small entrance port. The radiative limit of the V_{OC} (V_{OC-rad}) and the implied V_{OC} (V_{OC-imp}) were determined from the (intensity-dependent) PLQY measurements as described by Stolterfoht et al. [91] and Kirchartz et al. [133]. From the QFLS (E_F) one can calculate the "implied V_{OC}" via

$$V_{OC-imp} = \frac{\Delta E_F}{q} = V_{OC-rad} + \frac{k_B T}{q} \ln\left(\mathrm{PLQY}\frac{J_G}{J_{0-rad}}\right) \quad (2)$$

where V_{OC-rad} is the radiative limit, k_B the Boltzmann constant, T the temperature, q the elemental charge, J_G the generation current density, and J_{0-rad} the radiative thermal recombination current density in the dark. The internal ideality factor (n_{id}) was determined from these measurements as a fit to the calculated V_{OC-imp} [91, 92].

4.7 | Statistical Analysis

To check the deviation of the statistical results from each other, Welch's *t test* was applied. Welch's *t test* is an adaption of the Student's *t* test [82] and is more reliable when the two samples have unequal variances and possibly unequal sample sizes [136, 137]. These tests are often referred to as 'independent samples' or 'unpaired' *t* tests because they are usually applied when the statistics underlying the two samples being compared do not overlap. It is assumed that the sample means for the two samples being compared are normally distributed [82].

The *t* statistic for testing whether the results differ from each other or not can be calculated as follows.

$$t = \frac{\overline{X} - \overline{Y}}{\sqrt{\frac{S_x^2}{n_x} + \frac{S_y^2}{n_y}}} \quad (3)$$

whereas $\overline{X}$ and $\overline{Y}$ are the mean values, S_x and S_y the standard deviations, and n_x and n_y the sample sizes. The calculation was performed using a t test calculator [138].

PSCs with a V_{OC} below 0.8 V and a FF below 60% were excluded to filter out statistically irrelevant data.

Acknowledgments

The authors acknowledge the scientific discussions and the Si POLO bottom solar cells provided by ISFH (R. Peibst, S. Spätlich, M. Rienäcker) with funding of the program "zukunft.niedersachsen" by the Ministry of Science and Culture of the State of Lower Saxony (Project NextGenPV). The authors acknowledge the fruitful discussion and Si heterojunction bottom solar cell provided by CEA (P. Carroy) funded by the European Union. Views and opinions expressed are however those of the author(s) only and do not necessarily reflect those of the European Union or RIA. Neither the European Union nor the granting authority can be held responsible for them. NEXUS project has received funding from the European Union's Horizon Europe research and innovation program under grant agreement no. 101075330. Financial support by the Initiating and Networking funding of the Helmholtz Association (Project Zeitenwende and the Solar Technology Acceleration Platform (Solar TAP)), the program-oriented funding IV of the Helmholtz Association (Materials and Technologies for the Energy Transition, Topic 1: Photovoltaics and Wind Energy, Code: 38.01.04), the German Federal Ministry for Economic Affairs and Climate Action (BMWK) through the project 27Plus6 (03EE1056B), and the Karlsruhe School of Optics & Photonics (KSOP) are gratefully acknowledged. The authors thank the whole 'perovskite task force' at KIT for fruitful discussions and assistance. The help of Mohammad Gholipoor for making SEM images of textured 2T TSCs and Sören Ihssen for providing assistance with Python programming is acknowledged.

Open Access funding enabled and organized by Projekt DEAL.

Conflicts of Interest

The authors declare no conflicts of interest.

Data Availability Statement

The data that support the findings of this study are available from the corresponding author upon reasonable request.

References

1. A. Kojima, K. Teshima, Y. Shirai, and T. Miyasaka, *Journal of the American Chemical Society* 131 (2009): 6050.

2. Z. Liang, Y. Zhang, H. Xu, et al., *Nature* 624 (2023): 557.

3. "National Renewable Energy Laboratory," *Best Research-Cell Efficiency Chart*, accessed September, 2024, https://www.nrel.gov/pv/cell-efficiency.html.

4. T. Niewelt, B. Steinhauser, A. Richter, et al., *Solar Energy Materials and Solar Cells* 235 (2022): 111467.

5. C. Yang, W. Hu, J. Liu, et al., *Light: Science & Applications* 13 (2024): 1.

6. M. K. Rao, D. Sangeetha, M. Selvakumar, Y. Sudhakar, and M. Mahesha, *Solar Energy* 218 (2021): 469.

7. J.-P. Correa-Baena, M. Saliba, T. Buonassisi, et al., *Science* 358 (2017): 739.

8. D. Wang, M. Wright, N. K. Elumalai, and A. Uddin, *Solar Energy Materials and Solar Cells* 147 (2016): 255.

9. Y. Zheng, C. Tian, X. Wu, et al., *Advanced Energy Materials* 14 (2024): 20.

10. B. Conings, J. Drijkoningen, N. Gauquelin, et al., *Advanced Energy Materials* 5 (2015): 15.

11. E. J. Juarez-Perez, Z. Hawash, S. R. Raga, L. K. Ono, and Y. Qi, *Energy & Environmental Science* 9 (2016): 3406.

12. Z. Wang, Q. Lin, F. P. Chmiel, N. Sakai, L. M. Herz, and H. J. Snaith, *Nature Energy* 2 (2017): 9.

13. G. E. Eperon, S. D. Stranks, C. Menelaou, M. B. Johnston, L. M. Herz, and H. J. Snaith, *Energy & Environmental Science* 7 (2014): 982.

14. D. P. McMeekin, G. Sadoughi, W. Rehman, et al., *Science* 351 (2016): 151.

15. S. Gharibzadeh, P. Fassl, I. M. Hossain, et al., *Energy & Environmental Science* 14 (2021): 5875.

16. S. Akin, N. Arora, S. M. Zakeeruddin, M. Grätzel, R. H. Friend, and M. I. Dar, *Advanced Energy Materials* 10 (2019): 13.

17. E. Aydin, M. De Bastiani, and S. De Wolf, *Advanced Materials* 31 (2019): 25.

18. L. Fu, H. Li, L. Wang, R. Yin, B. Li, and L. Yin, *Energy & Environmental Science* 13 (2020): 4017.

19. F. Gao, Y. Zhao, X. Zhang, and J. You, *Advanced Energy Materials* 10 (2019): 13.

20. C. Liu, Y. Yang, H. Chen, et al., *Science* 382 (2023): 810.

21. S. Zhang, F. Ye, X. Wang, et al., *Science* 380 (2023): 404.

22. J. Warby, F. Zu, S. Zeiske, et al., *Advanced Energy Materials* 12 (2022): 2103567.

23. D. Menzel, A. Al-Ashouri, A. Tejada, et al., *Advanced Energy Materials* 12 (2022): 2201109.

24. Y. Shao, Y. Fang, T. Li, et al., *Energy & Environmental Science* 9 (2016): 1752.

25. J. S. Yun, J. Seidel, J. Kim, et al., *Advanced Energy Materials* 6 (2016): 13.

26. L. Liu, S. Huang, Y. Lu, et al., *Advanced Materials* 30 (2018): 29.

27. C. Ran, J. Xu, W. Gao, C. Huang, and S. Dou, *Chemical Society Reviews* 47 (2018): 4581.

28. S. G. Motti, D. Meggiolaro, A. J. Barker, et al., *Nature Photonics* 13 (2019): 532.

29. N. Phung, A. Al-Ashouri, S. Meloni, et al., *Advanced Energy Materials* 10 (2020): 20.

30. L. McGovern, I. Koschany, G. Grimaldi, L. A. Muscarella, and B. Ehrler, *Journal of Physical Chemistry Letters* 12 (2021): 2423.

31. Z. Fang, J. Sun, S. Liu, and L. Ding, *Journal of Semiconductors* 44 (2023): 080201.

32. R. Pappenberger, A. Diercks, J. Petry, S. Moghadamzadeh, P. Fassl, and U. W. Paetzold, *Advanced Functional Materials* 34 (2023): 9.

33. A. Al-Ashouri, E. Köhnen, B. Li, et al., *Science* 370 (2020): 1300.

34. M. Stolterfoht, P. Caprioglio, C. M. Wolff, et al., *Energy & Environmental Science* 12 (2019): 2778.

35. J. Xu, C. C. Boyd, Z. J. Yu, et al., *Science* 367 (2020): 1097.

36. F. Peña-Camargo, P. Caprioglio, F. Zu, et al., *ACS Energy Letters* 5 (2020): 2728.

37. J. Dagar, M. Fenske, A. Al-Ashouri, et al., *ACS Applied Materials & Interfaces* 13 (2021): 13022.

38. Y. Hou, E. Aydin, M. D. Bastiani, et al., *Science* 367 (2020): 1135.

39. E. Aydin, E. Ugur, B. K. Yildirim, et al., *Nature* 623 (2023): 732.

40. P. Tockhorn, J. Sutter, A. Cruz, et al., *Nature Nanotechnology* 17 (2022): 1214.

41. S.-G. Choi, S.-K. Jung, J.-H. Lee, J.-H. Kim, W. Zheng, and J.-W. Lee, *ACS Energy Letters* 9 (2024): 5360–5363.

42. B. Li and W. Zhang, *Communications Materials* 3 (2022): 1.

43. S. Hu, K. Otsuka, R. Murdey, et al., *Energy & Environmental Science* 15 (2022): 2096.

44. C. Quarti, F. De Angelis, and D. Beljonne, *Chemistry of Materials* 29 (2017): 958.

45. H. Chen, A. Maxwell, C. Li, et al., *Nature* 613 (2022): 676.

46. Y.-W. Jang, S. Lee, K. M. Yeom, et al., *Nature Energy* 6 (2021): 63.

47. S. Sidhik, Y. Wang, M. De Siena, et al., *Science* 377 (2022): 1425.

48. A. R. B. Mohd Yusoff, M. Vasilopoulou, D. G. Georgiadou, L. C. Palilis, A. Abate, and M. K. Nazeeruddin, *Energy & Environmental Science* 14 (2021): 2906.

49. X. Xu, Y.-M. Xie, Y. Ma, et al., *Solar RRL* 3 (2019): 8.

50. X. Zheng, Y. Hou, C. Bao, et al., *Nature Energy* 5 (2020): 131.

51. S. Akin, B. Dong, L. Pfeifer, Y. Liu, M. Grätzel, and A. Hagfeldt, *Advanced Science* 8 (2021): 10.

52. T. Duong, H. Pham, T. C. Kho, et al., *Advanced Energy Materials* 10 (2020): 9.

53. D. S. Lee, J. S. Yun, J. Kim, et al., *ACS Energy Letters* 3 (2018): 647.

54. J.-W. Lee, Z. Dai, T.-H. Han, et al., *Nature Communications* 9 (2018): 1.

55. M. Jung, T. J. Shin, J. Seo, G. Kim, and S. I. Seok, *Energy & Environmental Science* 11 (2018): 2188.

56. D. H. Kim, C. P. Muzzillo, J. Tong, et al., *Joule* 3 (2019): 1734.

57. C. Fei, M. Zhou, J. Ogle, D.-M. Smilgies, L. Whittaker-Brooks, and H. Wang, *Journal of Materials Chemistry A* 7 (2019): 23739.

58. L. Cheng, K. Meng, Z. Qiao, et al., *Advanced Materials* 34 (2021): 4.

59. S. Ahmad, P. Fu, S. Yu, et al., *Joule* 3 (2019): 794.

60. H. Yu, Y. Xie, J. Zhang, et al., *Advanced Science* 8 (2021): 12.

61. Y. Zheng, T. Niu, J. Qiu, et al., *Solar RRL* 3 (2019): 9.

62. P. Huang, S. Kazim, M. Wang, and S. Ahmad, *ACS Energy Letters* 4 (2019): 2960.

63. Z. Xu, M. Chen, and S. F. Liu, *Journal of Physical Chemistry Letters* 10 (2019): 3670.

64. X. Li, Y. Fu, L. Pedesseau, et al., *Journal of the American Chemical Society* 142 (2020): 11486.

65. F. E. Subhan, A. D. Khan, A. D. Khan, N. Ullah, M. Imran, and M. Noman, *RSC Advances* 10 (2020): 26631.

66. M. De Bastiani, A. J. Mirabelli, Y. Hou, et al., *Nature Energy* 6 (2021): 167.

67. F. Gota, R. Schmager, A. Farag, and U. W. Paetzold, *Optics Express* 30 (2022): 14172.

68. W. Qarony, M. I. Hossain, V. Jovanov, A. Salleo, D. Knipp, and Y. H. Tsang, *ACS Applied Materials & Interfaces* 12 (2020): 15080.

69. A. S. Subbiah, F. H. Isikgor, C. T. Howells, et al., *ACS Energy Letters* 5 (2020): 3034.

70. F. H. Isikgor, F. Furlan, J. Liu, et al., *Joule* 5 (2021): 1566.

71. A. Farag, R. Schmager, P. Fassl, et al., *ACS Applied Energy Materials* 5 (2022): 6700.

72. A. Farag, P. Fassl, H. Hu, et al., *Advanced Functional Materials* 33 (2022): 3.

73. J. Liu, M. D. Bastiani, E. Aydin, et al., *Science* 377 (2022): 302.

74. E. Aydin, J. Liu, E. Ugur, et al., *Energy & Environmental Science* 14 (2021): 4377.

75. J. Wang, C. Gao, X. Wang, et al., *Energy Technology* 9 (2020): 2000778.

76. X. Zheng, J. Liu, T. Liu, et al., *ACS Energy Letters* 7 (2022): 1987.

77. K. Sveinbjörnsson, B. Li, S. Mariotti, et al., *ACS Energy Letters* 7 (2022): 2654.

78. B. Chen, Z. J. Yu, S. Manzoor, et al., *Joule* 4 (2020): 850.

79. B. Chen, P. Wang, R. Li, et al., *ACS Energy Letters* 7 (2022): 2771.

80. Q. Li, Y. Zhao, W. Zhou, et al., *Advanced Energy Materials* 9 (2019): 1902239.

81. M. Kim, G.-H. Kim, T. K. Lee, et al., *Joule* 3 (2019): 2179.

82. B. L. Welch, *Biometrika* 34 (1947): 28.

83. M. A. Mahmud, T. Duong, Y. Yin, et al., *Advanced Functional Materials* 30 (2019): 7.

84. M. Malekshahi Byranvand, F. Behboodi-Sadabad, A. Alrhman Eliwi, et al., *Journal of Materials Chemistry A* 8 (2020): 20122.

85. J. Peng, D. Walter, Y. Ren, et al., *Science* 371 (2021): 390.

86. S. Li, Z. Liu, Z. Qiao, et al., *Advanced Functional Materials* 30 (2020): 52.

87. L. Zhang, Q. Kang, H. Shi, et al., *Solar RRL* 5 (2021): 8.

88. S. Sidhik, I. Metcalf, W. Li, et al., *Science* 384 (2024): 1227.

89. J. Wang, Y. Wu, J. Zhao, et al., *Small Methods* 8 (2024): 2400043.

90. J. Heo, S. W. Lee, J. Yong, et al., *Chemical Engineering Journal* 474 (2023): 145632.

91. M. Stolterfoht, M. Grischek, P. Caprioglio, et al., *Advanced Materials* 32 (2020): 2000080.

92. P. Fassl, V. Lami, F. J. Berger, et al., *Matter* 4 (2021): 1391.

93. S. Gharibzadeh, I. M. Hossain, P. Fassl, et al., *Advanced Functional Materials* 30 (2020): 1909919.

94. C. M. Wolff, S. A. Bourelle, L. Q. Phuong, et al., *Advanced Energy Materials* 11 (2021): 2101823.

95. N. Courtier, *Physical Review Applied* 14 (2020): 024031.

96. M. A. Green and A. W. Y. Ho-Baillie, *ACS Energy Letters* 4 (2019): 1639.

97. B. G. H. M. Groeneveld, S. Adjokatse, O. Nazarenko, et al., *Energy Technology* 8 (2019): 4.

98. D. Prochowicz, R. Runjhun, M. M. Tavakoli, et al., *Chemistry of Materials* 31 (2019): 1620.

99. G. Zeng, G. Liu, and X. Li, *ACS Sustainable Chemistry & Engineering* 11 (2023): 7664.

100. J. Wang, L. Yuan, H. Luo, et al., *Chemical Engineering Journal* 446 (2022): 136968.

101. W. Ke, C. Chen, I. Spanopoulos, et al., *Journal of the American Chemical Society* 142 (2020): 15049.

102. N. Yan, X. Ren, Z. Fang, et al., *Advanced Functional Materials* 32 (2022): 27.

103. H. Tsai, W. Nie, J.-C. Blancon, et al., *Nature* 536 (2016): 312.

104. X. Zhang, G. Wu, W. Fu, et al., *Advanced Energy Materials* 8 (2018): 14.

105. T. Niu, Y.-M. Xie, Q. Xue, et al., *Advanced Energy Materials* 12 (2021): 2.

106. F. Lang, O. Shargaieva, V. V. Brus, H. C. Neitzert, J. Rappich, and N. H. Nickel, *Advanced Materials* 30 (2017): 3.

107. S.-W. Lee, S. Kim, S. Bae, et al., *Scientific Reports* 6 (2016): 1.

108. N.-K. Kim, Y. H. Min, S. Noh, et al., *Scientific Reports* 7 (2017): 1.

109. J. A. Schwenzer, L. Rakocevic, R. Gehlhaar, et al., *ACS Applied Materials & Interfaces* 10 (2018): 16390.

110. P. Holzhey, P. Yadav, S.-H. Turren-Cruz, et al., *Materials Today* 29 (2019): 10.

111. J. Yang, B. D. Siempelkamp, D. Liu, and T. L. Kelly, *ACS Nano* 9 (2015): 1955.

112. D. Bryant, N. Aristidou, S. Pont, et al., *Energy & Environmental Science* 9 (2016): 1655.

113. J. M. Howard, E. M. Tennyson, S. Barik, et al., *Journal of Physical Chemistry Letters* 9 (2018): 3463.

114. K. Domanski, E. A. Alharbi, A. Hagfeldt, M. Grätzel, and W. Tress, *Nature Energy* 3 (2018): 61.

115. M. V. Khenkin, M. A.K., E. A. Katz, and I. Visoly-Fisher, *Energy & Environmental Science* 12 (2019): 550.

116. S. Bae, S. Kim, S.-W. Lee, et al., *Journal of Physical Chemistry Letters* 7 (2016): 3091.

117. M. V. Khenkin, E. A. Katz, A. Abate, et al., *Nature Energy* 5 (2020): 35.

118. X. Zheng, B. Chen, M. Yang, et al., *ACS Energy Letters* 1 (2016): 424.

119. S. Shao, J. Liu, H.-H. Fang, et al., *Advanced Energy Materials* 7 (2017): 22.

120. R. Singh, H. Hu, T. Feeney, et al., *ACS Applied Materials & Interfaces* 16 (2024): 27450.

121. C. Kan, P. Hang, S. Wang, et al., *Nature Photonics* 19, no. 1 (2024): 63.

122. F. Sahli, J. Werner, B. A. Kamino, et al., *Nature Materials* 17 (2018): 820.

123. P. K. Basu, A. Khanna, and Z. Hameiri, *Renewable Energy* 78 (2015): 590.

124. P. K. Basu, D. Sarangi, K. D. Shetty, and M. B. Boreland, *Solar Energy Materials and Solar Cells* 113 (2013): 37.

125. S. C. Baker-Finch and K. R. McIntosh, *Progress in Photovoltaics: Research and Applications* 21 (2012): 960.

126. A. Alasfour, Z. J. Yu, W. Weigand, D. Quispe, and Z. C. Holman, *Solar Energy Materials and Solar Cells* 218 (2020): 110761.

127. K. Wang, C. Liu, P. Du, et al., *Organic Electronics* 21 (2015): 19.

128. J. Chen, L. Zuo, Y. Zhang, et al., *Advanced Energy Materials* 8 (2018): 23.

129. M. Rai, L. H. Wong, and L. Etgar, *Journal of Physical Chemistry Letters* 11 (2020): 8189.

130. B. Chen, S.-W. Baek, Y. Hou, et al., *Nature Communications* 11 (2020): 1.

131. Q. Ye, W. Hu, J. Zhu, et al., *Energy & Environmental Science* 17, no. 16 (2024): 5866.

132. E. Gutierrez-Partida, H. Hempel, S. Caicedo-Dávila, et al., *ACS Energy Letters* 6 (2021): 1045.

133. L. Krückemeier, U. Rau, M. Stolterfoht, and T. Kirchartz, *Advanced Energy Materials* 10 (2020): 1902573.

134. J. C. Fischer, C. Li, S. Hamer, et al., *Advanced Materials Interfaces* 10 (2023): 11.

135. Z. Jiang, *Journal of Applied Crystallography* 48 (2015): 917.

136. G. D. Ruxton, *Behavioral Ecology* 17 (2006): 688.

137. B. Derrick and P. White, *The Quantitative Methods for Psychology* 12 (2016): 30.

138. "Dotmatics, Graphpad: T Test Calculator," accessed: September 2014, https://www.graphpad.com/quickcalcs/ttest1/?format=C.

Supporting Information

Additional supporting information can be found online in the Supporting Information section.